



Cite this: *Nanoscale*, 2021, **13**, 6184

## Optically tunable ultra-fast resistive switching in lead-free methyl-ammonium bismuth iodide perovskite films†

Swapnadeep Poddar,‡ Yuting Zhang,‡ Yiyi Zhu, Qianpeng Zhang and Zhiyong Fan \*

Resistive RAMs (Re-RAMs) have come to the fore as a rising star among the next generation non-volatile memories with fast operational speed, excellent endurance and prolonged data retention capabilities. Re-RAMs are being profusely used as storage and processing modules in neuromorphic hardware and high frequency switches in radio-frequency (RF) circuits. Owing to its intrinsic hysteresis and abundance of charge migration pathways, lead halide perovskites have emerged as a promising switching medium in Re-RAMs besides their ubiquitous usage in optoelectronic devices. Here, we adopted a lead-free eco-friendly methyl-ammonium bismuth iodide (MA<sub>3</sub>Bi<sub>2</sub>I<sub>9</sub>) perovskite (prepared by solvent-free engineering) as the switching medium sandwiched between copper (Cu) and indium doped tin oxide (ITO) electrodes. The devices exhibited a 10<sup>4</sup> high ON/OFF ratio that provided a large window for the multi-bit data storage in a single cell with good accuracy. Robust endurance of 1730 cycles and good data retention ability of >3 × 10<sup>5</sup> s were also observed. Careful switching speed measurements showed the devices can operate with an ultra-fast speed of 10 ns for writing and erasing respectively. The devices responded to light illumination and the prolonged retention of the opto-electrically tuned resistance states paved the way for image memorization.

Received 31st December 2020,  
Accepted 19th February 2021

DOI: 10.1039/d0nr09234g

rsc.li/nanoscale

### Introduction

Recently, resistive RAMs (Re-RAMs) have surfaced as a major promising contender for prospective non-volatile memories, neuromorphic computing hardware and high-speed radio-frequency (RF) circuits because of their robust temporal data retention, excellent cyclic endurance, mechanistic emulation of synaptic behaviour and ultra-fast operational speed.<sup>1–3</sup> A Re-RAM cell typically comprises an insulating/semiconducting layer (traditionally chalcogenides, oxides, selenides and nitrides) sandwiched between two metal electrodes, acting as the conducting pathway that triggers resistance change and hence consequent storage of data.<sup>4</sup> After its extensive fame in the genre of optoelectronics,<sup>5–10</sup> halide perovskite materials have also carved a niche for themselves in the field of Re-RAM, lately.<sup>11–16</sup> Innate hysteresis coupled with ubiquitous charge migration pathways render halide perovskites to be ideal can-

didates for the active resistive switching layer in Re-RAMs.<sup>17,18</sup> Compared to traditional Re-RAM switching layers that require complicated and sophisticated deposition processes,<sup>19</sup> halide perovskites (mostly the hybrid organic–inorganic ones) can be prepared by low temperature and hassle-free deposition techniques.<sup>20,21</sup> Although some previous reports have explored perovskite for photonic synapses,<sup>22</sup> pristine image memorization with perovskite Re-RAM and more specifically with toxicity-free perovskite Re-RAM, utilizing the intrinsic photo-responsive behaviour of perovskite has rarely been reported to the best of our knowledge.

In this work we fabricated a Re-RAM device comprising methyl-ammonium bismuth iodide (MBI or MA<sub>3</sub>Bi<sub>2</sub>I<sub>9</sub>) perovskite sandwiched between translucent copper (Cu) and transparent indium doped tin oxide (ITO) electrodes. The MBI perovskite was chosen particularly to address the concern of toxicity in traditional lead (Pb) halide perovskites.<sup>23,24</sup> The MBI layer was fabricated by a two-step vapour deposition technique (deposition of metallic bismuth by thermal evaporation followed by chemical vapour deposition of methyl-ammonium iodide resulting in the MBI film. For details see the Methods section). The devices exhibited resistive switching characteristics with a sturdy ON/OFF ratio of 10<sup>4</sup> enabling a large window for multiple resistance levels. Careful mechanistic

Department of Electronic & Computer Engineering, The Hong Kong University of Science and Technology, Clear Water Bay, Kowloon, Hong Kong SAR, China.

E-mail: eezfan@ust.hk

†Electronic supplementary information (ESI) available. See DOI: 10.1039/d0nr09234g

‡These authors contributed equally to this work.

study demonstrated the dominance of metallic Cu ion intrusion and subsequent reduction within the bulk of the perovskite to be the dominant cause of switching. The MBI Re-RAMs showed temporal data retention of resistance state in the order of  $>3 \times 10^5$  s and robust electrical endurance of 1730 cycles. Ultra-fast writing and erasing speed of 10 ns were observed for the MBI Re-RAMs. This is the fastest reported switching speed in Re-RAMs based on perovskite thin-films to the best of our knowledge.<sup>25</sup> On being illuminated by a 100 mW cm<sup>-2</sup> light source, the devices demonstrated zero-bias current response and coupled with larger electrical stimulation (0.5 V), the optoelectrically maneuvered resistance states could be retained for  $1.1 \times 10^4$  s. As a concept proof, we selectively lit up a diagonal pattern in a  $5 \times 5$  square matrix array and illustrated the temporal retention of the pattern.

## Results and discussion

Fig. 1a (left) shows the device structure of the MBI Re-RAM. The MBI layer (prepared by solvent-free engineering. See the Methods section) was deposited on a clean transparent indium-doped tin oxide (ITO) glass. The top electrode was deposited in the form of 30 nm thick translucent rectangular copper bars (each 500  $\mu$ m wide). Fig. 1a (right) shows a representative schematic of the electrical and photo-response of the MBI Re-RAM. The output 'D' is high when there is either light input or positive electrical input (equivalent to writing) or both w.r.t. the Cu electrode. For the rest of the cases with a negative electrical input (equivalent to erasing), output 'D' is always low. Hence the resultant logic output for the MBI Re-

RAM is effectively  $D = (A + B)\bar{C}$ , where A, B and C are the optical, electrical writing and electrical erasing inputs, respectively. The photoluminescence (PL) spectrum of the MBI layer has been presented in Fig. 1b. The PL intensity peaks at 630 nm which is consistent with the previous reports on thin-film based MBI systems.<sup>26</sup> The Tauc-plot obtained from ultraviolet-visible spectroscopy (UV-Vis) and the ultraviolet photoelectron spectroscopy (UPS) have been presented in ESI Fig. S1a.† The optical bandgap was confirmed to be 2.1 eV for the MBI perovskite used in our Re-RAM and is also consistent with previous reports.<sup>26</sup> It is to be noted here that the mismatch or Stokes shift in the peak PL intensity as seen from Fig. 1b, relative to the energy bandgap value obtained from the Tauc plot in Fig. S1a† (by 40 nm) can be explained by the presence of inter-band trap states in polycrystalline perovskite and subsequent trapping of photo-generated electrons by them.<sup>27</sup> The valence band maxima (VBM) and the conduction band minima (CBM): -5.74 eV and -3.74 eV as obtained from Fig. S1b,† match closely with previously reported MBI VBM and CBM of -6.08 eV and -3.96 eV respectively.<sup>28</sup>

The top-view SEM of the MBI film formed by solvent-free engineering has been shown in Fig. 1c. The polycrystalline morphology and the individual grain boundaries of the MBI film are well visible. The hexagonal grains can be as large as 1  $\mu$ m in lateral dimension. Fig. 1d represents the cross-sectional SEM image of the MBI film deposited on ITO glass. The conformal MBI layer has been highlighted in blue and the ITO in pink. The layer on top of the MBI is a protective sheath of platinum (Pt) metal deposited while trimming the sample with a focused ion beam (for details see Methods section). As seen in Fig. 1e, the peaks of the X-ray diffraction (XRD) spectrum

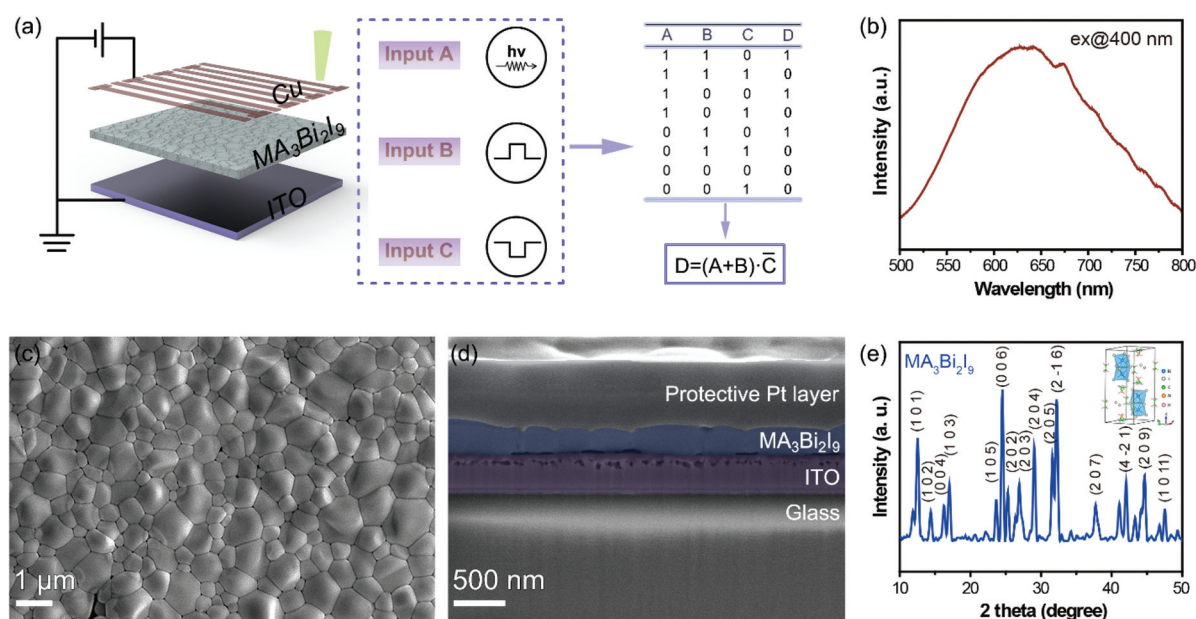


**Fig. 1** Device structure and material characterization. (a) Schematic showing the structure of the MBI Re-RAM device (left). Tabular illustration of response of the MBI Re-RAM device to electrical and optical inputs (right). (b) PL spectrum of the MBI perovskite film on ITO glass. (c) Top-view SEM image exhibiting the hexagonal morphology of the polycrystalline MBI perovskite. (d) Cross-sectional SEM image of MBI perovskite on ITO glass, prepared by focused ion beam trimming. (e) XRD spectrum of the MBI perovskite. Inset shows the crystal structure of the MBI perovskite.

match well with that of the previously reported MBI thin films.<sup>29–33</sup> Also, the inset plot of Fig. 1e shows the crystal structure of the MBI perovskite.

Fig. 2a shows the  $I$ - $V$  characteristics of the MBI Re-RAM. Cyclic voltage sweeps were run from 0 V  $\rightarrow$  3 V  $\rightarrow$  -9 V  $\rightarrow$  0 V (w.r.t. Cu electrode) without any current compliance. The device switched from the high resistance state (HRS) to the low resistance state (LRS) at 1.8 V and jumped back to the HRS at -8 V for the first cycle of operation. The consecutive stabilized operational  $I$ - $V$  cycles however demonstrated a much lower threshold voltage (1 V for writing and -6.4 V) for switching indicating an underlying filamentary mechanism.<sup>34</sup> The variation of the ON/OFF current and threshold writing and erasing voltage have been duly shown in Fig. S2 of the ESI.† In Fig. 2b, the HRS and LRS current values of the MBI Re-RAM devices for different device areas have been plotted. Devices with areas 0.0016 mm<sup>2</sup>, 1.2 mm<sup>2</sup>, 2.5 mm<sup>2</sup> and 7.06 mm<sup>2</sup> were fabricated on the same chip. Although the HRS current decreased more or less monotonically with the reduction in device dimension, the LRS current did not scale down with the device size insinuating a typical electrochemical metallization behaviour in the MBI Re-RAM.<sup>35</sup> To further confirm the possible dominant role of copper in MBI Re-RAM switching, we carried out secondary-mass ion spectroscopy (SIMS) study on the devices. Two devices were used; one switched to the LRS and one was kept un-switched at the HRS. Following the electrical operation on the devices, positive polarity SIMS was conducted on the

devices by bombarding the MBI Re-RAM with primary oxygen (O<sub>2</sub>) ions. A sputtering area of 0.12 mm<sup>2</sup> and sputtering energy of 3 keV were used. As seen in Fig. 2c, the intensity of the secondary Cu ions (Cu<sup>+</sup>), as analysed using a SIMS analyser, was manifold times higher within the bulk perovskite for the switched device compared to the un-switched device. This conclusively proved the pervasion of Cu inside the bulk MBI film resulting in filament formation and consequent switching. It must be mentioned here that apart from ECM based perovskite Re-RAMs demonstrating switching with active metal electrodes,<sup>34,36</sup> previous reports on halide perovskite Re-RAM have also demonstrated the valence change mechanism (VCM) type of switching with inert electrodes.<sup>37,38</sup> In those studies, the switching in perovskite has been attributed to the halide vacancies formed within the switching layer. However, with an active metal like Cu as the top electrode, and direct evidence of Cu intrusion in the perovskite film, we propose the following ECM dominant hypothesis for MBI Re-RAM as schematically demonstrated in Fig. 2d-f. Fig. 2d shows the MBI Re-RAM to be in the HRS in the sub-threshold regime. With the application of the positive voltage, the anodized Cu ions move into the MBI film and so do the electrons from the ITO side. As shown in Fig. 2e, upon reaching the writing threshold electric field, the electrically reduced Cu starts to electro-crystallize and hence the current starts rising sharply. Once the two electrodes, Cu and ITO are bridged, the transformation to the LRS is complete.<sup>39</sup> Opposite polarity voltage coupled with excessive

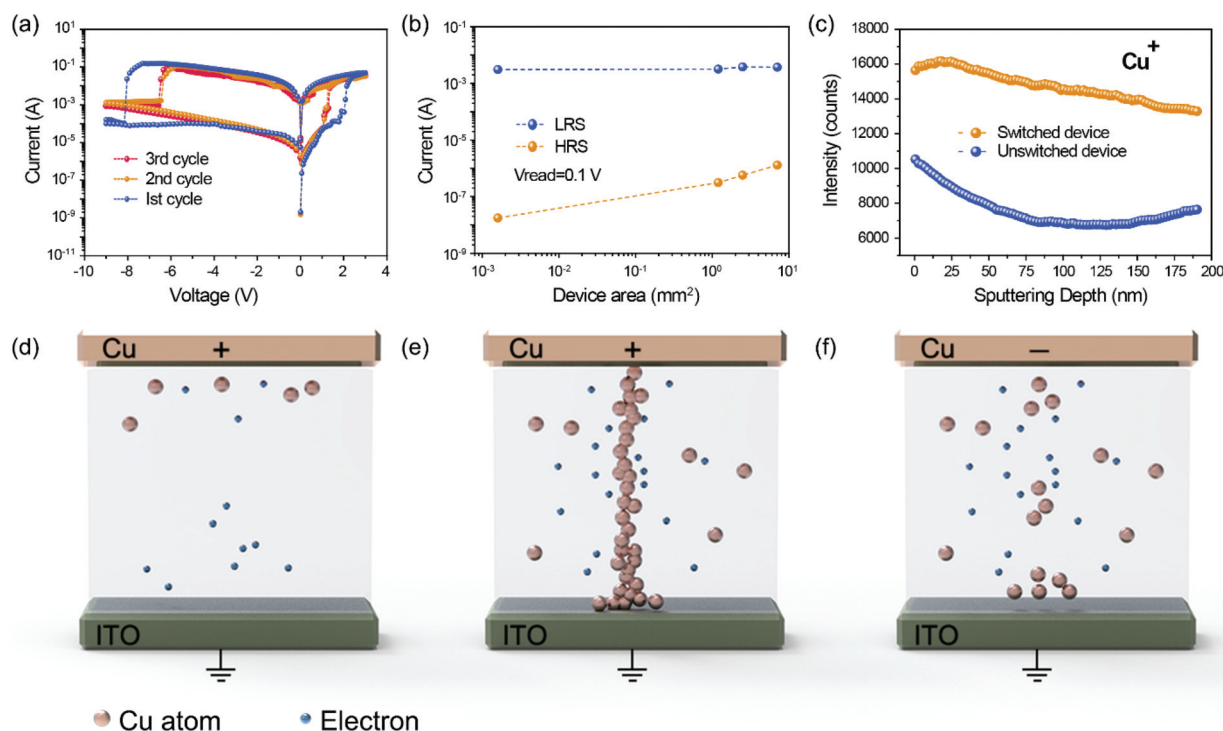


**Fig. 2** Electrical characterization and working principle of the MBI Re-RAM device. (a)  $I$ - $V$  characteristics of the MBI Re-RAM device. (b) Plot showing HRS and LRS current values of MBI Re-RAM at a reading voltage of 0.1 V for different device dimensions. (c) Plot showing the intensity of secondary Cu ions obtained by SIMS study on switched and un-switched MBI Re-RAM devices. (d-f) Schematic illustrating the working principle of MBI Re-RAM based on electrochemical metallization of Cu.

Joule heating ruptures the Cu filament to render the system back to the HRS as shown in Fig. 2f.

Fig. 3a shows the endurance performance of the MBI Re-RAM signifying its electrical robustness. A pulse train comprising write/read/erase/read pulses of 10 V/0.1 V/−10 V/0.1 V amplitude was used. The pulse width used for all the pulses was 10 ms. The device showed excellent endurance performance of 1730 cycles without any degradation of the ON/OFF ratio following which the device demonstrated abrupt transformation from the LRS to HRS. The cumulative density function (CDF) plot for the device endurance demonstrating the distribution of data points and isolation of HRS/LRS is shown in Fig. S3 of the ESI.†

Another very important device characterization metric is the temporal data retention ability of the device. In order to measure the retention time of the MBI Re-RAM devices, the devices were SET to the LRS with a positive half of the  $I$ - $V$  scan ( $0\text{ V} \rightarrow 8\text{ V} \rightarrow 0\text{ V}$ ) and then the resistance state was monitored with a continuous DC biasing voltage of 0.1 V. In order to obtain the HRS, the device SET to the LRS was erased with a negative half of the  $I$ - $V$  scan ( $0\text{ V} \rightarrow -8\text{ V} \rightarrow 0\text{ V}$ ) and the HRS was subsequently monitored with a DC biasing voltage of 0.1 V. A current compliance of  $10^{-2}\text{ A}$  was used during the above-mentioned  $I$ - $V$  scans to prevent the breakdown of the device. As seen from Fig. 3b, the MBI Re-RAM devices exhibited temporal retention of data for  $>3 \times 10^5\text{ s}$ .

Fig. 3c shows that the MBI Re-RAM device possesses the ability to allow multiple resistance states to store multiple bits of data in a single memory cell. Three different current compliances were chosen for the electrical  $I$ - $V$  scans ( $0\text{ V} \rightarrow 8\text{ V} \rightarrow -8\text{ V} \rightarrow 0\text{ V}$ ) namely  $10^{-5}\text{ A}$ ,  $10^{-4}\text{ A}$  and  $10^{-3}\text{ A}$  respectively. The different current compliances used gave rise to three distinctly different LRSs demonstrating the multi-bit data storage capability. Note, it can be distinctly observed here that the erasing or RESET voltage reduces with the reduction of current compliance which is another typical trait of filamentary Re-RAM systems.<sup>40</sup> Lower current injection indicates a lower number of filamentary pathways and less energy is required to rupture the filaments. To show further, we chose six individual devices and operated them under  $I$ - $V$  scan mode ( $0\text{ V} \rightarrow 8\text{ V} \rightarrow -8\text{ V} \rightarrow 0\text{ V}$ ). Each of those six devices yielded a distinct HRS and LRS every time for each compliance operated upon. The three distinct LRSs and one distinct HRS thus obtained have been illustrated in Fig. 3d. This shows the possibility of at least four states or two bits of data storage for a single cell. We also used the pulse mode of operation to demonstrate the multi-bit storage capability. A pulse train comprising varying writing and constant reading and erasing voltage pulses were fed to the MBI Re-RAM device. The voltage schemes used were (7 V/0.1 V/−10 V/0.1 V), (8 V/0.1 V/−10 V/0.1 V), (9 V/0.1 V/−10 V/0.1 V) and (10 V/0.1 V/−10 V/0.1 V) respectively. Each of the different writing voltage pulses resulted in different LRS

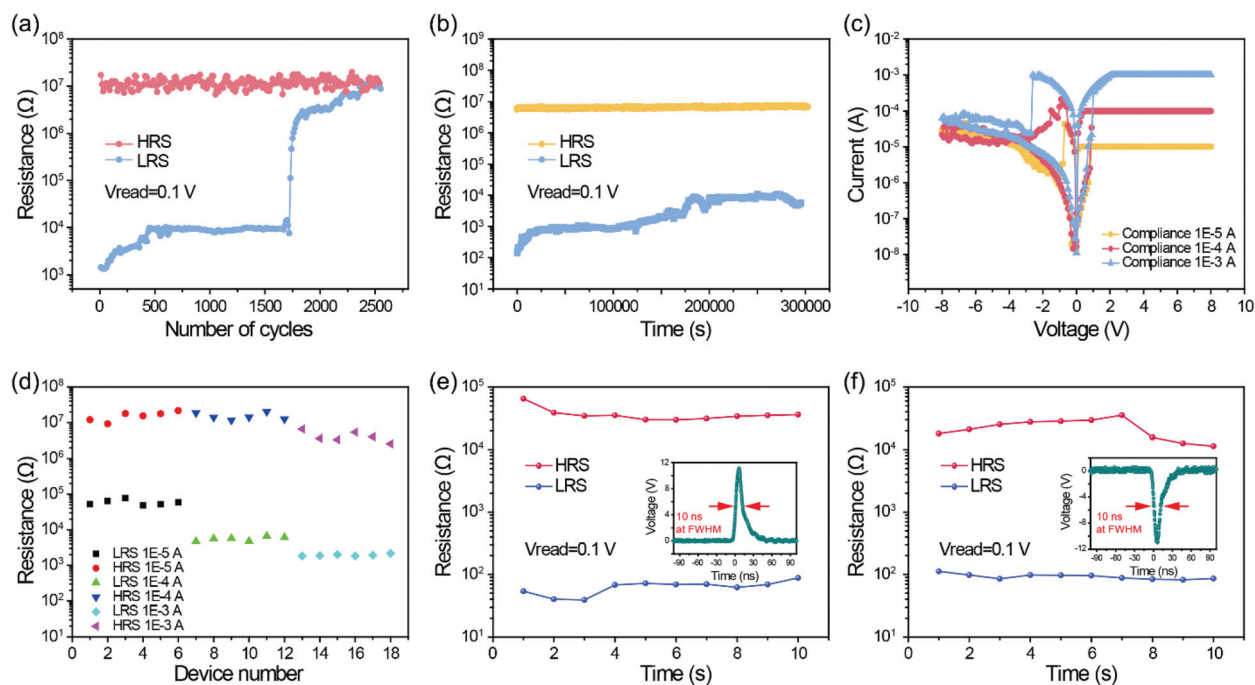


**Fig. 3** Evaluation of performance metrics for the MBI Re-RAM device. (a) Plot showing endurance performance of MBI Re-RAM at a reading voltage of 0.1 V. (b) Plot showing temporal retention ability of the MBI Re-RAM device at a reading voltage of 0.1 V. (c) Plot showing the  $I$ - $V$  characteristics of MBI Re-RAM when operated under varying current compliances. (d) Plot showing the distinct resistance levels obtained by operating under  $10^{-3}\text{ A}$ ,  $10^{-4}\text{ A}$  and  $10^{-5}\text{ A}$  current compliances thereby exhibiting possibility of multi-level data storage in a single MBI Re-RAM memory cell. (e) Plot showing the before and after (HRS and LRS) resistance levels of MBI Re-RAM when excited with 10 ns, 10 V writing pulse. Inset shows the input writing voltage pulse. (f) Plot showing the before and after (LRS and HRS) resistance levels of MBI Re-RAM when excited with 10 ns, −10 V erasing pulse. Inset shows the input erasing voltage pulse.

current (0.55 mA, 0.82 mA, 1.17 mA and 1.8 mA respectively for 7 V, 8 V, 9 V and 10 V respectively) when the devices were read with a reading voltage pulse of amplitude 0.1 V as can be seen from ESI Fig. S4.† This further corroborates the feasibility of two bit storage for a single MBI Re-RAM device.

Device operational speed is a key figure-of-merit for any non-volatile memory. In order to investigate the writing speed of the MBI Re-RAM, the device was fed with a single 10 ns wide and 10 V amplitude pulse and the resistance of the device was monitored before and after the application of the pulse with a reading voltage of 0.1 V. As seen from Fig. 3e, the resistance of the device changed from  $10^5 \Omega$  (shown by red line) to  $10^4 \Omega$  (blue line) upon application of a single pulse. Similarly for deciphering the erasing speed, a  $-10$  V amplitude and 10 ns wide pulse were fed to the device already in the LRS. The device showed transition from  $10^2 \Omega$  (shown by blue line) to  $10^4 \Omega$  (shown in red line) as demonstrated in Fig. 3f. To the best of our knowledge, this is the fastest speed ever reported for any thin-film perovskite Re-RAM device.<sup>25</sup> The ultra-fast device operational speed can be ascribed to the highly mobile Cu ions and the fast moving electrons supplied by the ITO counter electrode, within the bulk of the perovskite, resulting in super-fast filament formation/rupture processes.

Halide perovskites, already famous in the domain of optoelectronics and photovoltaics have been used recently as optoelectronic resistive switching memories and photonic

synapses.<sup>22</sup> However, as far as we know, MBI perovskite has not yet been explored for optoelectronic resistive switching applications. The MBI Re-RAM device was operated in the  $I$ - $V$  scan mode ( $0 \text{ V} \rightarrow 2 \text{ V}/6 \text{ V} \rightarrow -9 \text{ V} \rightarrow 0 \text{ V}$ ) without any current compliance under both light and dark conditions. A light source of intensity of  $100 \text{ mW cm}^{-2}$  was used for the illumination of the device. The  $I$ - $V$  characteristics have been plotted in Fig. 4a for the light (blue line) and dark (red line) cases. The device in the dark switched from HRS to LRS at 1 V and from LRS to HRS at  $-6.9 \text{ V}$ . The device under illumination, however, exhibited switching at 0.4 V and erasing at  $-6.1 \text{ V}$ . The reduced threshold writing voltage can be ascribed to the enhanced photo-generated electrons and the consequent lowering of required electrical energy for reducing incoming metallic Cu ions and hence filament formation. However it is interesting to note that, the LRS resistance state thus achieved required lower electrical energy for erasing or transformation to the HRS when compared to the device in the dark. A plausible explanation for that could be innate instability or weaker retention of the optically maneuvered LRS level compared to the ones obtained by pristine electrical stimulation. Coupled with that, the prolonged illumination of  $100 \text{ mW cm}^{-2}$  light can result in Joule heating which adds to the electrical energy required for erasing thereby lowering the threshold voltage. Fig. 4b shows the output current of the MBI Re-RAM when operated with zero biasing voltage. When the  $100 \text{ mW cm}^{-2}$

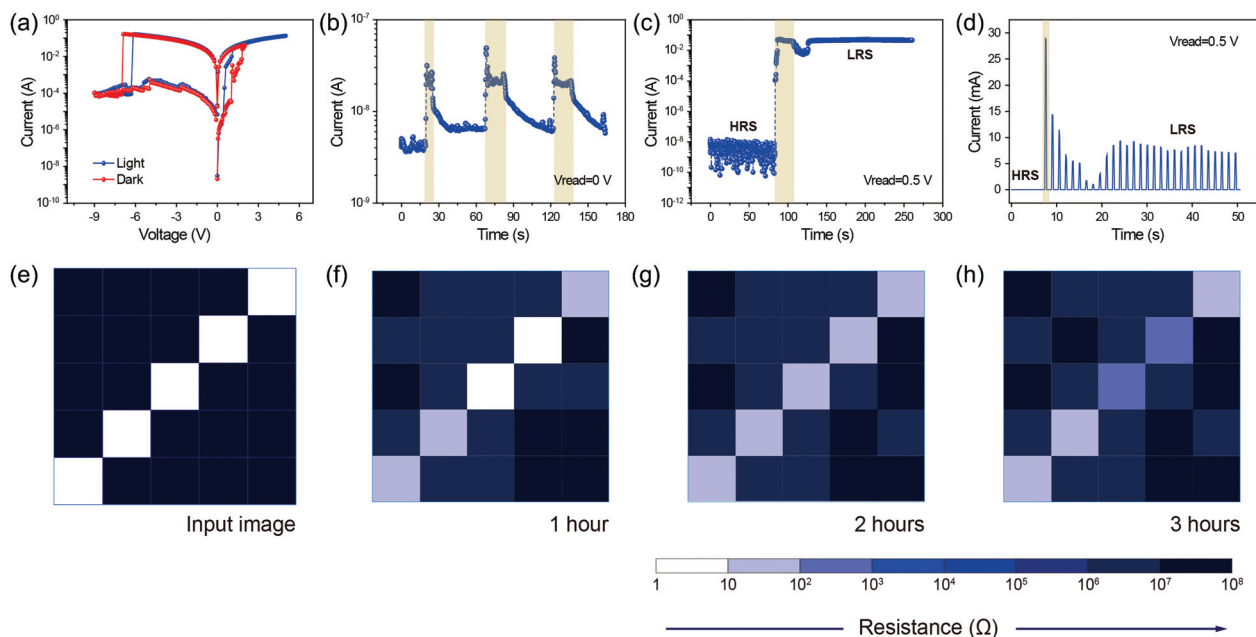


**Fig. 4** Opto-electrical memorization in the MBI Re-RAM device. (a)  $I$ - $V$  characteristics of the MBI Re-RAM device under light and dark conditions. (b) Plot showing the photo-response of the MBI Re-RAM device at zero bias. (c) Plot showing the photo-response of MBI Re-RAM at 0.5 V DC biasing voltage w.r.t the Cu electrode. (d) Plot showing the photo-response of MBI Re-RAM at 0.5 V pulse biasing voltage w.r.t the Cu electrode. The yellow bars in (b-d) demonstrate the duration of illumination. (e) Schematic showing the input image for the  $5 \times 5$  square matrix array demonstrating image memorization in MBI Re-RAM. (f) Matrix plot showing the resistance levels of individual devices in the  $5 \times 5$  square matrix array after one hour of image storage. (g) Matrix plot showing the resistance levels of individual devices in the  $5 \times 5$  square matrix array after two hours of image storage. (h) Matrix plot showing the resistance levels of individual devices in the  $5 \times 5$  square matrix array after three hours of image storage. The scale bar for tracing the resistance levels for (f-h) is shown at the bottom right.

illumination is on, the device current increases from the HRS to a quasi-LRS by 6–7 times. However, when the light shining is not there, the optically tuned current level cannot be temporally maintained with zero biasing. As seen from Fig. 4c, when we increased the device reading voltage to 0.5 V, the device still stayed at the HRS. The moment the light was ON, the device jumped from the HRS to LRS demonstrating a change in current by  $10^6$  orders of magnitude. Even after the light was put off, the device maintained the LRS with an electrical reading bias of 0.5 V. Similarly, in Fig. 4d, upon being operated by electrical pulses of 0.5 V amplitude and 150 ms width, the MBI Re-RAM showed opto-electric switching similar to the DC biasing case in Fig. 4c. After the illumination was removed, the current plummeted a little followed by a rise and stabilization. This trend may be explained by the sudden absence of photo-generated electrons once the light is turned off, resulting in current drop succeeded by the dissipation of high-intensity light induced Joule heating rendering the current to rise and stabilize consequently aiding the LRS to be retained for long time. In order to get an idea of the retention ability of the optically tuned LRSs, we fabricated a  $5 \times 5$  MBI Re-RAM device array and stored a diagonal pattern of five squares illuminated by  $100 \text{ mW cm}^{-2}$  light as can be seen from Fig. 4e–h. The five squares forming the diagonal of the square matrix were switched to the LRS from HRS one by one with a DC biasing voltage of 0.5 V similar to that in Fig. 4c. The retention time of the image thus stored in the square matrix was monitored every hour for three hours by a reading voltage of 0.1 V. The memorized image could be successfully stored for 3 hours (see Fig. 4f–h). The temporal retention ability profile of a single MBI Re-RAM device exhibiting data storage for  $1.1 \times 10^4 \text{ s}$  is provided in ESI Fig. S5a.† Therefore it could be empirically confirmed that the resistance state obtained by coupled optical and sub-threshold electrical stimulation could not be retained as long as the one obtained purely by electrical stimulation ( $3 \times 10^5$  as shown in Fig. 3b) ESI Fig. S5b.† shows the impact of prolonged illumination on the optically tuned LRS of the MBI Re-RAM device. The device gradually jumped from the LRS to HRS at a read-out bias of 0.5 V when it was subjected to prolonged illumination over 100 s. This erasing upon extended illumination is attributed to the excessive Joule heating caused by high intensity light, rupturing the metallic Cu filament bridging the Cu and ITO electrodes. This again is consistent with the reduced threshold erasing voltage reported in Fig. 4a. Device to device variation data for the opto-electric switching in MBI Re-RAM are provided in ESI Fig. S6a–d.†

## Conclusions

In this work, a lead-free eco-friendly MBI perovskite has been used as an active switching layer in ECM dominant Re-RAM comprising a conducting path formed from metallic Cu. The devices demonstrated robust switching characteristics namely 1730 cycles of electrical endurance,  $3 \times 10^5 \text{ s}$  of data

retention capability and ON/OFF ratio of  $10^4$ . The MBI Re-RAM devices accommodate at least four distinct resistance states and consequently at least two bits of data in a single memory cell thereby paving the way for high density storage. The devices exhibited exceptionally fast writing and erasing speed, the best among reported perovskite thin film Re-RAMs so far. The MBI Re-RAMs showed a response to  $100 \text{ mW cm}^{-2}$  light illumination. The devices could transform from the HRS to LRS at small readout electrical readout voltage, when subjected to light illumination. As a concept proof, we also demonstrated the storing of an image (a diagonal in a  $5 \times 5$  square matrix) and successfully monitored the temporal retention without any significant degradation of data. All in all, the MBI-Re RAM proposed here will pave the way for high speed opto-electrically tunable and electrically stable Re-RAMs for future embedded electronics, RF circuits, neuromorphic computing hardware and wearable electronic devices requiring memory modules.

## Materials

Methyl-ammonium-iodide (MAI) powder was purchased from Dyesol.

## Methods

### Device fabrication

Indium-doped tin oxide (ITO) coated clean glasses were used as the bottom electrode for the MBI Re-RAM device. The sheet resistance of the ITO layer was  $20 \Omega$ . 20 nm thick metallic bismuth (Bi) was evaporated on the ITO coated glass by the thermal evaporation technique at a deposition rate of  $1 \text{ \AA}$  per second. Following this, chemical vapour deposition (CVD) was carried out for perovskite growth. A quartz boat containing MAI powder was used as the source in a single zone CVD furnace. The Bi deposited ITO coated glass was placed on the upper open face of the quartz boat such that the Bi deposited side faced the MAI powder maintaining an air gap of 0.5 cm. The deposition temperature of  $185 \text{ }^\circ\text{C}$  was used and argon (Ar) gas was flowed in at the rate of 200 sccm. The CVD process, carried out for 25 minutes, ensured complete reaction between metallic Bi and MAI precursor and yielded a polycrystalline MBI film with a thickness of 200–250 nm. Following the CVD process, the thermal evaporation of translucent 30 nm thick Cu electrodes was carried out. Devices with areas  $0.0016 \text{ mm}^2$ ,  $1.2 \text{ mm}^2$ ,  $2.5 \text{ mm}^2$  and  $7.06 \text{ mm}^2$  were fabricated for the electrical and optical measurements.

### Material characterization

The PL emission spectrum was obtained using a FLS920P fluorescence spectrometer. The absorbance wavelength spectrum (UV-Vis) was obtained using a Varian Cary 500 spectrometer (Varian, USA) and FLS920P fluorescence spectrometer. The

ultraviolet photoelectron spectroscopy (UPS) measurement of the MBI film was carried out using an Axis Ultra DLD using Kratos Axis Ultra DLD multi-technique surface analysis system. The study of the crystal structure (XRD) of MBI film was done using a Bruker D8 X-ray diffractometer. The cross-sectional SEM samples of the MBI film were prepared using a dual-beam FEI Helios G4 UX FIB/FESEM system. A protective layer of platinum (Pt) was deposited on the MBI film using a voltage of 2 kV and a current of 6.4 nA. After that, a regular cross-sectional cutting tool (RCS) and cleaning cross sectional cutting tool (CCS) were used at a voltage of 15 kV (both for RCS and CCS) and current of 2.4 nA and 1.2 nA respectively for RCS and CCS in order to obtain the cross-section of the MBI film. Both the cross-sectional and top-view images of the MBI film were captured in the FESEM mode of the dual-beam FEI Helios G4 UX FIB/FESEM system. The Secondary Mass Ion Spectroscopy of the MBI Re-RAM was done by ToF SIMS V (ION-TOF GmbH).

### Device characterization

The electrical characterization of the devices was carried out using a Keithley 2450 source meter assisted by home-built LABVIEW programs. Single electrical pulse used for device operational speed measurement was generated using an Agilent 8112A pulse generator and the waveform thus generated was traced using a high-speed DPO 4104B digital phosphor oscilloscope.

### Author contributions

Z. Fan, S. Poddar and Y. Zhang conceptualized the experiments and analysed the results. Y. Zhu helped with PL, XRD and UPS measurements. Q. Zhang helped with device fabrication. All authors participated in writing and articulating the manuscript.

### Data and materials availability

Additional data required for supporting the work may be obtained from the author upon reasonable request.

### Funding

This work was supported by the National Natural Science Foundation of China (project 51672231), the General Research Fund (Project No. 16309018, 16214619) from the Hong Kong Research Grant Council, the HKUST Fund of Nanhai (grant number FSNH-18FYTRI01), Shenzhen Science and Technology Innovation Commission (Project No. JCYJ20180306174923335, JCYJ20170818114107730). The authors also acknowledge the support from the Center for 1D/2D Quantum Materials and State Key Laboratory of Advanced Displays and Optoelectronics Technologies at HKUST.

### Conflicts of interest

The authors declare no competing interest.

### Acknowledgements

The authors thank Dr Yuan Cai from Material and Characterization Preparation Facility (MCPF) at HKUST for her help with the Focused Ion Beam operation. The authors also thank He Huang for drawing the MBI crystal structure. The authors also express gratitude to Prof. Lu Tao Weng from HKUST MCPF for assisting with the SIMS study. The authors thank MCPF and Nanofabrication Facility (NFF) at HKUST for technical support.

### Notes and references

- 1 S. Goswami, A. J. Matula, S. P. Rath, S. Hedström, S. Saha, M. Annamalai, D. Sengupta, A. Patra, S. Ghosh and H. Jani, *Nat. Mater.*, 2017, **16**, 1216.
- 2 K. Moon, S. Lim, J. Park, C. Sung, S. Oh, J. Woo, J. Lee and H. Hwang, *Faraday Discuss.*, 2019, **213**, 421–451.
- 3 M. Kim, R. Ge, X. Wu, X. Lan, J. Tice, J. C. Lee and D. Akinwande, *Nat. Commun.*, 2018, **9**, 1–7.
- 4 H. Wang and X. Yan, *Phys. Status Solidi RRL*, 2019, **13**, 1900073.
- 5 L. Gu, S. Poddar, Y. Lin, Z. Long, D. Zhang, Q. Zhang, L. Shu, X. Qiu, M. Kam and A. Javey, *Nature*, 2020, **581**, 278–282.
- 6 M. M. Tavakoli, K.-H. Tsui, Q. Zhang, J. He, Y. Yao, D. Li and Z. Fan, *ACS Nano*, 2015, **9**, 10287–10295.
- 7 A. Waleed, M. M. Tavakoli, L. Gu, Z. Wang, D. Zhang, A. Manikandan, Q. Zhang, R. Zhang, Y.-L. Chueh and Z. Fan, *Nano Lett.*, 2017, **17**, 523–530.
- 8 Q. Zhang, D. Zhang, L. Gu, K.-H. Tsui, S. Poddar, Y. Fu, L. Shu and Z. Fan, *ACS Nano*, 2020, **14**, 1577–1585.
- 9 X. Zheng, Z. Wei, H. Chen, Q. Zhang, H. He, S. Xiao, Z. Fan, K. S. Wong and S. Yang, *Nanoscale*, 2016, **8**, 6393–6402.
- 10 A. Waleed and Z. Fan, *Sci. Bull.*, 2017, **62**, 645–647.
- 11 C. Zuo, H. J. Bolink, H. Han, J. Huang, D. Cahen and L. Ding, *Adv. Sci.*, 2016, **3**, 1500324.
- 12 H. Kim, J. S. Han, S. G. Kim, S. Y. Kim and H. W. Jang, *J. Mater. Chem. C*, 2019, **7**, 5226–5234.
- 13 F. Zeng, Y. Guo, W. Hu, Y. Tan, X. Zhang, J. Feng and X. Tang, *ACS Appl. Mater. Interfaces*, 2020, **12**, 23094–23101.
- 14 W. H. Qian, X. F. Cheng, Y. Y. Zhao, J. Zhou, J. H. He, H. Li, Q. F. Xu, N. J. Li, D. Y. Chen and J. M. Lu, *Adv. Mater.*, 2019, **31**, 1806424.
- 15 X. F. Cheng, W. H. Qian, J. Wang, C. Yu, J. H. He, H. Li, Q. F. Xu, D. Y. Chen, N. J. Li and J. M. Lu, *Small*, 2019, **15**, 1905731.
- 16 W. H. Qian, X. F. Cheng, J. Zhou, J. H. He, H. Li, Q. F. Xu, N. J. Li, D. Y. Chen, Z. G. Yao and J. M. Lu, *InfoMat*, 2020, **2**, 743–751.

- 17 Z. Xu, Z. Liu, Y. Huang, G. Zheng, Q. Chen and H. Zhou, *J. Mater. Chem. C*, 2017, **5**, 5810–5817.
- 18 C. Eames, J. M. Frost, P. R. Barnes, B. C. O'regan, A. Walsh and M. S. Islam, *Nat. Commun.*, 2015, **6**, 7497.
- 19 Y. Li, S. Long, M. Zhang, Q. Liu, L. Shao, S. Zhang, Y. Wang, Q. Zuo, S. Liu and M. Liu, *IEEE Electron Device Lett.*, 2010, **31**, 117–119.
- 20 J. You, Z. Hong, Y. Yang, Q. Chen, M. Cai, T.-B. Song, C.-C. Chen, S. Lu, Y. Liu and H. Zhou, *ACS Nano*, 2014, **8**, 1674–1680.
- 21 M. R. Leyden, L. K. Ono, S. R. Raga, Y. Kato, S. Wang and Y. Qi, *J. Mater. Chem. A*, 2014, **2**, 18742–18745.
- 22 Y. Wang, Z. Lv, Q. Liao, H. Shan, J. Chen, Y. Zhou, L. Zhou, X. Chen, V. A. Roy and Z. Wang, *Adv. Mater.*, 2018, **30**, 1800327.
- 23 S. M. Jain, T. Edvinsson and J. R. Durrant, *Commun. Chem.*, 2019, **2**, 1–7.
- 24 L. Zhang, K. Wang and B. Zou, *ChemSusChem*, 2019, **12**, 1612–1630.
- 25 B. Hwang and J.-S. Lee, *Nanoscale*, 2018, **10**, 8578–8584.
- 26 B. W. Park, B. Philippe, X. Zhang, H. Rensmo, G. Boschloo and E. M. Johansson, *Adv. Mater.*, 2015, **27**, 6806–6813.
- 27 S. Li, J. Luo, J. Liu and J. Tang, *J. Phys. Chem. Lett.*, 2019, **10**, 1999–2007.
- 28 C. Momblona, H. Kanda, A. A. Sutanto, M. Mensi, C. Roldán-Carmona and M. K. Nazeeruddin, *Sci. Rep.*, 2020, **10**, 1–8.
- 29 J. K. Pious, M. Lekshmi, C. Muthu, R. Rakhi and V. C. Nair, *ACS Omega*, 2017, **2**, 5798–5802.
- 30 M. Pazoki, M. B. Johansson, H. Zhu, P. Broqvist, T. Edvinsson, G. Boschloo and E. M. Johansson, *J. Phys. Chem. C*, 2016, **120**, 29039–29046.
- 31 S. Tie, W. Zhao, D. Xin, M. Zhang, J. Long, Q. Chen, X. Zheng, J. Zhu and W. H. Zhang, *Adv. Mater.*, 2020, **32**, 2001981.
- 32 K. Eckhardt, V. Bon, J. Getzschmann, J. Grothe, F. M. Wisser and S. Kaskel, *Chem. Commun.*, 2016, **52**, 3058–3060.
- 33 C. Ni, G. Hedley, J. Payne, V. Svrcek, C. McDonald, L. K. Jagadamma, P. Edwards, R. Martin, G. Jain and D. Carolan, *Nat. Commun.*, 2017, **8**, 1–7.
- 34 J. S. Han, Q. V. Le, J. Choi, K. Hong, C. W. Moon, T. L. Kim, H. Kim, S. Y. Kim and H. W. Jang, *Adv. Funct. Mater.*, 2018, **28**, 1705783.
- 35 H. Ling, M. Yi, M. Nagai, L. Xie, L. Wang, B. Hu and W. Huang, *Adv. Mater.*, 2017, **29**, 1701333.
- 36 J. Choi, Q. V. Le, K. Hong, C. W. Moon, J. S. Han, K. C. Kwon, P.-R. Cha, Y. Kwon, S. Y. Kim and H. W. Jang, *ACS Appl. Mater. Interfaces*, 2017, **9**, 30764–30771.
- 37 C. Gu and J.-S. Lee, *ACS Nano*, 2016, **10**, 5413–5418.
- 38 X. Zhu, J. Lee and W. D. Lu, *Adv. Mater.*, 2017, **29**, 1700527.
- 39 R. Waser, R. Dittmann, G. Staikov and K. Szot, *Adv. Mater.*, 2009, **21**, 2632–2663.
- 40 Y. Zhang, H. Wu, Y. Bai, A. Chen, Z. Yu, J. Zhang and H. Qian, *Appl. Phys. Lett.*, 2013, **102**, 233502.